metals

MDPI

Article

Effects of Ceramic Particulate Type and Porosity on the Corrosion Behavior of Open-Cell AlSn6Cu Composites Produced via Liquid-State Processing

Mihail Kolev [1,*], Vanya Dyakova [1,2], Yoanna Kostova [1], Boriana Tzaneva [2,3], Hristina Spasova [1] and Rositza Dimitrova [1]

[1] Institute of Metal Science, Equipment and Technologies with Hydro- and Aerodynamics Centre "Acad. A. Balevski", Bulgarian Academy of Sciences, Shipchenski Prohod Str., 67, 1574 Sofia, Bulgaria; v_diakova@ims.bas.bg (V.D.); y_kostova@ims.bas.bg (Y.K.); h.spasova@ims.bas.bg (H.S.); rossy@ims.bas.bg (R.D.)

[2] National Center for Mechatronics and Clean Technologies, 8 "Kliment Ohridski" Blvd., Building 8, 1756 Sofia, Bulgaria; borianatz@tu-sofia.bg

[3] Department of Chemistry, Technical University of Sofia, Kliment Ohridski Blvd. 8, 1000 Sofia, Bulgaria

* Correspondence: mihail1kolev@ims.bas.bg

Abstract

The corrosion behavior of open-cell AlSn6Cu-based composites, one reinforced with SiC particles and the other with Al_2O_3 particles, was investigated. The composites were fabricated via liquid-state processing, employing both squeeze casting and the replication method, and they produced in two distinct pore size ranges (800–1000 μm and 1000–1200 μm). Corrosion performance was systematically evaluated through gravimetric (weight loss) measurements and electrochemical techniques, including open-circuit potential monitoring and potentiodynamic polarization tests. Comprehensive microstructural and phase analyses were conducted using X-ray diffraction, energy-dispersive X-ray spectroscopy, and scanning electron microscopy. The results revealed that both reinforcement type and pore architecture have a significant impact on corrosion resistance. Al_2O_3-reinforced composites consistently outperformed their SiC-containing counterparts, and pore enlargement generally improved performance for the unreinforced alloy and the Al_2O_3 composite but not for the SiC composite. Overall, the optimal corrosion resistance is achieved by pairing a coarser-pore architecture (1000–1200 μm) with Al_2O_3 reinforcement, which minimizes both instantaneous (electrochemical) and cumulative (gravimetric) corrosion metrics. This study addresses a gap in current research by providing the first detailed assessment of corrosion in open-cell AlSn6Cu-based composites with controlled pore architectures and different ceramic reinforcements, offering valuable insights for the development of advanced lightweight materials for harsh environments.

Keywords: open-cell AlSn6Cu composites; corrosion behavior; SiC; Al_2O_3

check for updates

Academic Editors: Wislei Riuper Osório and Ausdinir Danilo Bortolozo

Received: 4 July 2025
Revised: 19 September 2025
Accepted: 21 September 2025
Published: 25 September 2025

Citation: Kolev, M.; Dyakova, V.; Kostova, Y.; Tzaneva, B.; Spasova, H.; Dimitrova, R. Effects of Ceramic Particulate Type and Porosity on the Corrosion Behavior of Open-Cell AlSn6Cu Composites Produced via Liquid-State Processing. *Metals* **2025**, *15*, 1073. https://doi.org/10.3390/met15101073

Copyright: © 2025 by the authors. Licensee MDPI, Basel, Switzerland. This article is an open access article distributed under the terms and conditions of the Creative Commons Attribution (CC BY) license (https://creativecommons.org/licenses/by/4.0/).

1. Introduction

Open-cell Al-based metal matrix composites are extensively investigated owing to their low density, high specific strength, excellent energy absorption capacity, and superior thermal and acoustic insulation, making them attractive for automotive, aerospace, biomedical, and energy-related applications [1–3].

The performance of such composites, particularly with respect to mechanical and tribological properties, is further enhanced by the incorporation of various reinforcing

particles, including carbides, oxides, nitrides, borides, carbon-based materials, and even certain waste-derived reinforcements. A wide range of reinforcements is explored, such as B_4C [4], TiC [5–7], graphite, and graphene [8,9], each providing distinct property improvements, including increased hardness, enhanced thermal conductivity, or self-lubricating effects. Among these, however, SiC [10–12] and Al_2O_3 [13–15] remain the most widely used reinforcements due to their proven effectiveness in significantly improving the hardness and wear resistance of aluminum matrix composites, thereby making them particularly attractive for advanced engineering applications.

While the addition of reinforcement particles generally improves the mechanical properties of composites, it also has adverse effects on their corrosion resistance. The porous morphology strongly influences corrosion behavior. High specific surface areas and open-cell structures facilitate the penetration of aggressive environments, leading to localized corrosion. In aluminum foams, the protective Al_2O_3 passive film is disrupted by stress concentrations and micropores, promoting pitting, crevice corrosion, and in some cases, galvanic corrosion, particularly in the presence of reinforcing particles or surface coatings [16–18]. Corrosion behavior depends on pore size, surface treatments, and reinforcement type: larger pores generally reduce corrosion by improving electrolyte circulation, surface treatments stabilize the passive film, while nanoparticles such as Al_2O_3 can reduce the corrosion rate [1,17–19].

The mechanisms governing corrosion in composites are often dictated by the chemical and electrochemical properties of both the matrix and the reinforcements [20]. For instance, while Al_2O_3 and boron-based compounds are electrical insulators, SiC is a semiconductor, and graphite (Gr) is a conductor; thus, galvanic reactions typically occur only between aluminum and conductive reinforcements such as carbon. Nevertheless, another study also reports galvanic corrosion in Al–B and Al–SiC composites [21].

The underlying mechanisms of corrosion in SiC-reinforced composites remain diverse and result in different conclusions across studies. The corrosion behavior of Al–SiC composites with varying SiC contents is examined by electrochemical testing in HCl and NaCl solutions [22], and the effect of SiC particle size is also investigated [23]. Microgalvanic coupling between the aluminum matrix and SiC particles is identified as a factor that reduces corrosion resistance [24]. In contrast, other studies demonstrate that Al–SiC composites exhibit improved corrosion resistance compared with pure aluminum [25]. Furthermore, increasing the volume fraction of SiC particles also enhances the corrosion resistance of Al–SiC composites [26].

Studies examine the corrosion behavior of Al–Al_2O_3 composites with different reinforcement contents in H_2SO_4 and NaCl solutions, and the highest corrosion rates occur in mixed H_2SO_4 + NaCl electrolytes [27]. Increasing the Al_2O_3 content up to 10 wt.% improves corrosion resistance due to the formation of a protective oxide layer that preserves the composite surface passivity [28].

Despite extensive research on aluminum matrix composites and the effects of different reinforcements, the literature still lacks systematic studies on the corrosion behavior of open-cell AlSn6Cu-based composites. Recent investigations on AlSn6Cu reinforced with SiC [29] and Al_2O_3 [30] demonstrate that ceramic particles influence the mechanical and tribological performance. However, no systematic studies address the corrosion performance of open-cell AlSn6Cu–SiC and AlSn6Cu–Al_2O_3 composites under controlled pore architectures and fabricated by liquid-state processing.

The aim of this study is to evaluate the corrosion behavior of open-cell AlSn6Cu composites reinforced with SiC or Al_2O_3 and produced with controlled pore sizes (800–1000 μm and 1000–1200 μm). This work assesses corrosion resistance using gravimetric and electrochemical methods supported by microstructural and phase characterization (XRD, EDS,

SEM). This study provides the first systematic assessment of corrosion in these novel composites, complementing earlier tribological investigations [29,30]. This unique focus on corrosion behavior fills an important gap in the literature, as previous research has not established how pore morphology and reinforcement type govern corrosion resistance in these materials. By addressing this gap, the study provides insights that are essential for the reliable design and application of open-cell AlSn6Cu composites in corrosive service environments.

2. Materials and Methods

2.1. Production Method and Materials

The matrix alloy employed in this study was AlSn6Cu, with a nominal composition of 5.5–6.5 wt.% Sn, 1.3–1.7 wt.% Cu, 0.2 wt.% Ni, 0.3 wt.% Si, and the remainder Al. Spherical Al_2O_3 and SiC particles with particle sizes of 300–400 μm were used as ceramic reinforcements at a fixed content of 5 wt.%. Sodium chloride (NaCl) particles in two size ranges (800–1000 μm and 1000–1200 μm) served as space holders to generate open porosity in the composites. The open-cell composites were fabricated via a liquid-state processing route, specifically squeeze casting combined with the salt replication method. The production technology parameters—such as reinforcement ratio, compaction pressure, thermal schedules, and infiltration conditions—were based on protocols optimized in previous studies [29,30]. Initially, the ceramic particles (Al_2O_3 or SiC) were thoroughly mixed with NaCl particles to achieve the desired 5 wt.% reinforcement in the final composite. This mixture was then cold-pressed into cylindrical green compacts under a uniaxial pressure of 100 MPa. The resulting green compacts were dried at 200 °C for 2 h to eliminate residual moisture, followed by sintering at 800 °C ± 1 °C for 1 h in air, then cooled to room temperature. The sintered preforms were preheated and placed into a steel mold, and molten AlSn6Cu alloy (at 680 °C ± 2 °C) was infiltrated using a squeeze casting process under a pressure of 80 MPa for 60 s. After solidification, the NaCl space-holder was removed by immersion in an ultrasonic cleaner containing distilled water at 79 °C, producing the open-cell composite structures. Any remaining salt was eliminated by repeated rinsing and subsequent drying at 120 °C. The open-cell architecture of the C (800–1000 μm pores) and E (1000–1200 μm pores) specimens is illustrated in the cross-sectional optical images and three-dimensional X-ray microtomography reconstructions shown in Figure 1. The three-dimensional X-ray microtomography analysis confirmed that both pore architectures are predominantly open and highly interconnected. For the C specimen, the total porosity was 66.1%, of which nearly the entire volume corresponded to open porosity (66.1%), with only a negligible closed porosity of 0.00145%. The object surface was measured as 1.38×10^3 mm^2, and the Euler number (−1518) demonstrates a strongly interconnected network of fine pores within a total analyzed volume of 317 mm^3. In comparison, the E specimen exhibited a total porosity of 58.1%, again almost entirely open (58.1%) with a very small closed porosity of 0.133%. The object surface was 9.76×10^3 mm^2, and the Euler number (−218) confirm an open but coarser pore structure within a total volume of 258 mm^3. These results verify that both composites possess true open-cell architectures, with the finer-pore specimen displaying a higher degree of connectivity relative to the coarse-pore specimen. The lower total porosity measured for the E specimen indicates that the larger pores are bounded by comparatively thicker walls, consistent with the cross-sectional images in Figure 1.

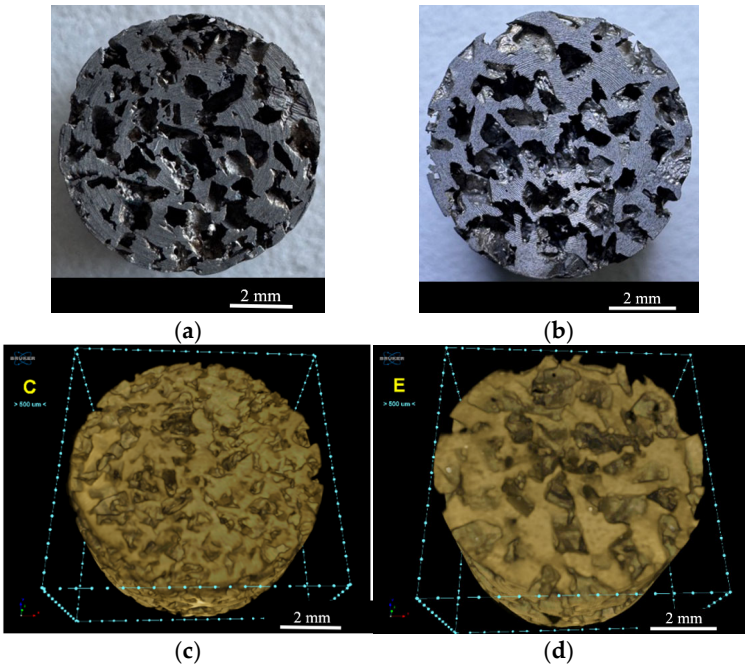

Figure 1. Cross-sectional optical images and three-dimensional X-ray microtomography reconstructions of open-cell AlSn6Cu composites: (**a**) optical cross-section of C specimen (800–1000 µm pores); (**b**) optical cross-section of E specimen (1000–1200 µm pores); (**c**) X-ray microtomography reconstruction of C specimen; (**d**) X-ray microtomography reconstruction of E specimen.

Figure 2 presents a schematic overview of the complete experimental workflow, encompassing composite fabrication, characterization, and corrosion testing procedures.

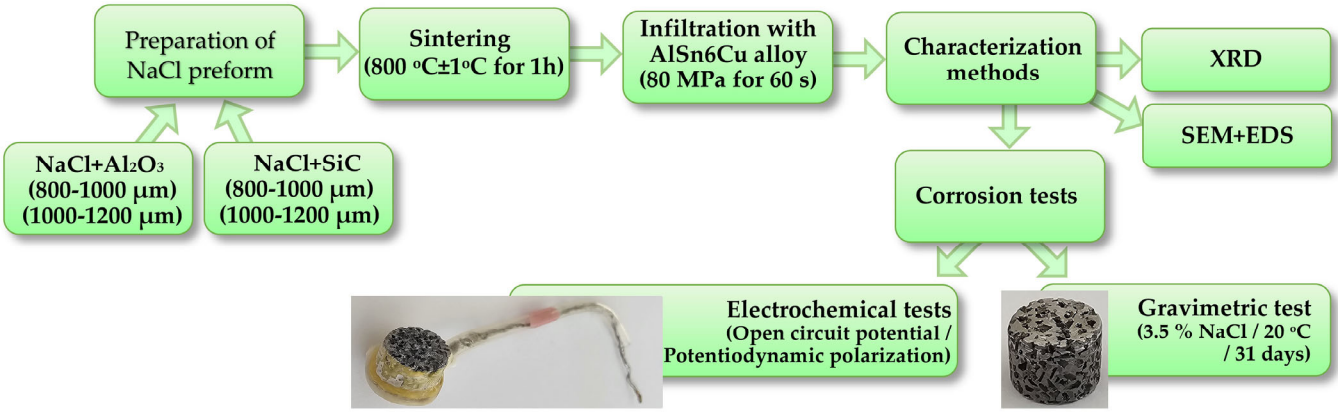

Figure 2. Schematic overview of the experimental workflow: open-cell AlSn6Cu-based composites fabrication, microstructural characterization, corrosion testing with general view of specimens and working electrode for electrochemical investigations.

For the corrosion experiments, six distinct types of open-cell composites were prepared, varying by both pore size and reinforcement type. Two pore size ranges were investigated: 800–1000 µm and 1000–1200 µm. Within each pore size range, specimens were fabricated with either no ceramic reinforcement, 5 wt.% SiC, or 5 wt.% Al_2O_3. Sample designations are: C and E (unreinforced with fine and coarse pores, respectively), SC and SE (SiC-reinforced with fine and coarse pores, respectively), and AC and AE (Al_2O_3-reinforced with fine and coarse pores, respectively). These designations are summarized in Table 1. This systematic approach allowed for a direct assessment of both the effects of ceramic reinforcement and pore size on the corrosion behavior of the open-cell AlSn6Cu-based composites.

Table 1. Total porosity, coefficient of roughness and corrosion-electrochemical parameters of the studied composites obtained from the polarization dependences in 3.5% NaCl. In parentheses are the results of the same samples, but with sealed pores.

Type of Composite	Pore Size [μm]	Designation	Archimedes Porosity [%]	Total Porosity [%]	Obj. S [cm^2]	Coefficient of Roughness R_f	OCP [V]	E_{corr} [V]	J_{corr} [μA cm^{-2}]	I_{pore}/I_{sealed}
AlSn6Cu	800–1000	C	64.0	65.5	13.8	4.49	−0.682 (−0.416)	−0.847 (−0.400)	10.6 ± 1.5	3.46
AlSn6Cu-SiC		SC	49.1	48.3	9.76	4.48	−0.903 (−0.645)	−0.903 (−0.619)	18.7 ± 2.7	1.71
AlSn6Cu-Al_2O_3		AC	45.9	45.5	16.9	4.41	−0.990 (−0.645)	−0.956 (−0.646)	11.4 ± 1.1	1.75
AlSn6Cu	1000–1200	E	53.7	55.8	15.1	4.19	−0.666 (−0.548)	−0.804 (−0.629)	4.8 ± 0.01	2.61
AlSn6Cu-SiC		SE	37.2	36.6	16.3	4.11	−1.173 (−0.607)	−1.103 (−0.591)	37.9 ± 2.4	4.87
AlSn6Cu-Al_2O_3		AE	38.7	37.6	15.1	4.12	−0.746 (−0.643)	−0.753 (−0.618)	4.01 ± 0.8	3.59

2.2. Characterization Methods

The phase composition of the open-cell AlSn6Cu–SiC and AlSn6Cu–Al_2O_3 composites after corrosion testing was analyzed by X-ray diffraction (XRD). Diffraction patterns were acquired using a TDM-10 X-ray diffractometer (Dandong Tongda Science and Technology Co., Ltd., Dandong, China) equipped with a scintillation detector and operating with Ni-filtered Cu Kα radiation at 35 kV and 30 mA. Data were collected over a 2θ range of 35–120°, with a step size of 0.01° and a scan rate of 0.3°/min. Phase identification was performed using the PDF-2 database (ICDD), and further analysis was conducted with MDI Jade 6.5 software.

The object surface area (Obj. S) and total porosity of the composites were quantified by three-dimensional analysis using a Skyscan 1272 X-ray microtomography (Bruker, Berlin, Germany). The system features an X-ray source focus of less than 5 μm at 4 W and a nominal resolution below 0.35 μm. The Obj. S parameter represents the cumulative surface area of all solid phases within the volume of interest (VOI), as determined by the marching cubes algorithm. The measurements were carried out at a source voltage of 100 kV and source current of 100 μA, with a pixel size of 13.0 μm and a resolution of 1632 × 1092 pixels over a 360° rotation. Image processing was performed using conditional mean filtering in 3D space (square kernel, radius 5, threshold 5), global thresholding (gray values 86–255), and despeckling (3D sweep, retaining only the largest object).

The morphology and elemental composition of the corrosion products were investigated by scanning electron microscopy (SEM) equipped with energy-dispersive X-ray spectroscopy (EDS). SEM/EDS analyses were performed on a HIROX 5500 instrument (HIROX Europe, Limonest, France) equipped with a BRUKER EXDS system (Bruker Co., Berlin, Germany) with the following parameters—maximum accelerating voltage 30 keV, emission current in secondary electron (SE) mode—120 μA, emission current in back-scattered electron (BSE) mode—110 μA.

2.3. Corrosion Test Methods

The corrosion behavior of two open-cell AlSn6Cu-based composites—one reinforced with SiC particles and the other with Al_2O_3 particles—was investigated using gravimetric and electrochemical methods. Nine specimens of each composite type were prepared according to ASTM G1 [31] and divided into three groups (n = 3).

Gravimetric tests were performed by immersing the specimens with cylindrical shape (Figure 1) continuously in 3.5 wt.% NaCl solution at 25 °C for a total of 31 days. Mass loss (Δm, %) was determined by weighing each specimen on an analytical balance before testing (m_0) and after removal of corrosion products (m_1). Measurements were recorded

after 12 days (group 1), 26 days (group 2), and 31 days (group 3), and Δm was calculated as presented in (1), where m_0 and m_1 are the mass of each sample before the corrosion test and after removal of the corrosion product:

$$\Delta m\% = \frac{m_0 - m_1}{m_0} \times 100 \quad (1)$$

The mass loss measurements for each of the three time periods were performed on different samples that were not reused.

Electrochemical tests began by monitoring the open-circuit potential (OCP) for 10 min in the same NaCl solution at room temperature, without deaeration. Potentiodynamic polarization was then carried out from −0.20 V to +0.25 V vs. OCP at a scan rate of 1 mV s^{-1}. This scan rate was chosen as the most optimal for studying complex systems such as aluminum alloys reinforced with SiC or Al_2O_3 [21,23,25,27]. On the one hand, the slower scan rate of 0.167 mV s^{-1} is considered to have minimal distorted around the corrosion potential [32], but in the case of valve metals the slow measurements lead to irreversible surface changes and the accumulation of corrosion products [33]. On the other hand, at faster scan rates (above 5 mV s^{-1}) the influence of the electrical double layer capacitance strongly collapses [33]. The current obtained was converted into current density using a roughness factor (R_f), which is a dimensionless quantity representing the ratio of real surface area to geometric surface area [34,35]. The real surface area (Obj. S) was obtained from tomographic analysis, while the geometric surface area is the area of the cylindrical sample used. The corrosion current density (J_{corr}) is determined from the intersection of the tangent lines to the anodic and cathodic branches in the Tafel regions of the polarization curves, which occurs at the corrosion potential. The error in determining the corrosion current density as a result of the distortion of the polarization dependences (at scan rate of 1 mV s^{-1}) is presented after the corresponding values in Table 1. All electrochemical measurements were performed in a three-electrode cell comprising an Ag/AgCl reference electrode, a platinum counter electrode, and the composite specimen as the working electrode. The working electrodes were made by fixing a copper conductor in a polyethylene tube to one side of the cylindrical specimen, after which the contact and the side walls were well insulated with duracryl and insulating varnish. After the tests, the working surface was also covered with duracryl to seal the pores and then polished in order to investigate the influence of the composite composition excluding the influence of the pores. A potentiostat/galvanostat PalmSens4 and PSTrace 5.11 software (PalmSens BV, Houten, The Netherlands) were used for the electrochemical tests.

3. Results

3.1. Electrochemical Measurement

The change in open circuit potential with time can be seen in Figure 3, and the values recorded at the tenth minute are presented in Table 1. The values of the open-circuit potentials for samples C and E are stable and very close to each other. The reinforcing additives to E to form composites AE and SE shift the OCP in the negative direction by about 80 and 500 mV, respectively. Reinforcement of composite C with carbide and oxide particles extends the time to reach a steady-state OCP value and shifts its values in the negative direction by about 220 and 310 mV, respectively. Therefore, in all cases of the reinforcing additives, an increase in surface activity can be expected, with the strongest negative effect being the addition of SiC to the composite with larger pores. The influence of the pore size and the type of reinforcing phase (SiC and Al_2O_3) on the potentiodynamic dependences of the composites are presented in Figure 4. From the polarization dependences, the main corrosion-electrochemical parameters such as corrosion potential (E_{corr}) and corrosion

current density (J_{corr}) were determined. The obtained values for these quantities, as well as total porosity and coefficient of roughness (R_f) are presented in Table 1.

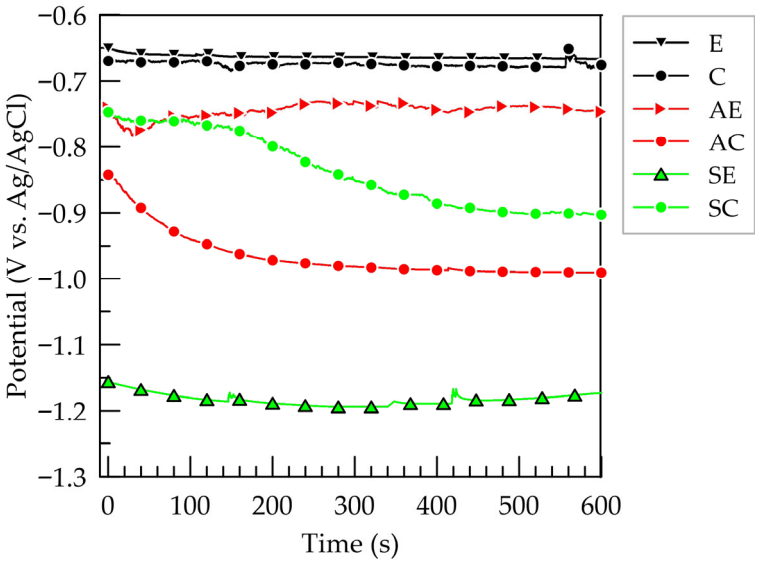

Figure 3. Open circuit potential vs. time for tested composites in 3.5% NaCl.

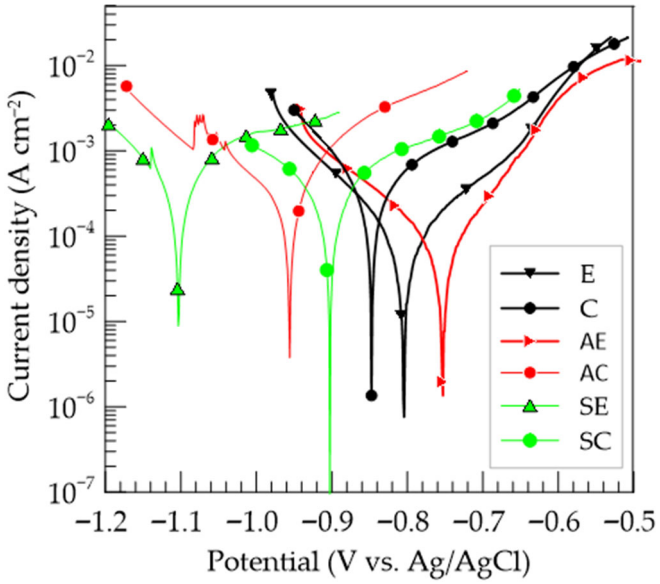

Figure 4. Polarization dependences of AlSn6Cu with different porosity and reinforcing additive of SiC or Al_2O_3 in 3.5% NaCl, scan rate 1 mV/s.

The corrosion-electrochemical response of the open-cell AlSn6Cu materials is governed by a complex interplay between surface roughness factor, pore architecture and reinforcement chemistry. Although the roughness coefficients ($R_f \approx 4.1$–4.5) vary by less than 9% across all specimens, the corresponding corrosion current densities ($J_{corr} \approx 4.0$–38 μA cm^{-2}) span almost an order of magnitude, indicating that geometric enlargement of the real surface is a secondary factor relative to microgalvanic effects introduced by the ceramic particles and the degree of electrolyte penetration dictated by pore size.

The unreinforced alloy (C) exhibits moderately negative potentials (OCP = −0.682 V, E_{corr} = −0.847 V) and a J_{corr} of 10.6 μA cm^{-2}. Adding SiC (SC) leaves roughness unchanged but drives both potentials ~0.22 V more negative and almost doubles J_{corr} to 18.7 μA cm^{-2}. This influence of SiC particles could be explained by their cathodic behavior with respect to the metal matrix and the formation of microgalvanic corrosion cell, stimulating the

dissolution of the surrounding metal. By contrast, Al_2O_3 reinforcement (AC) lowers roughness marginally; although OCP/E_{corr} shift further negative (≈−0.99/−0.96 V), J_{corr} rises only slightly to 11.4 μA cm^{-2}, implying that electrically insulating Al_2O_3 has a far milder influence on anodic kinetics than SiC.

For the unreinforced composites (E) the larger pores coincide with a lower roughness (4.19) and noticeably improved corrosion resistance (J_{corr} = 4.80 μA cm^{-2}). When SiC is introduced (SE), roughness falls further to 4.11, but OCP plunges to −1.173 V and J_{corr} surges to 37.9 μA cm^{-2}—the highest in the series—confirming again that galvanic interactions around SiC dominate the electrochemical behavior. The Al_2O_3-containing analog (AE) shows the lowest J_{corr} of all specimens (4.01 μA cm^{-2}) and potentials only slightly more negative than the unreinforced material (−0.746/−0.753 V), underscoring the benign character of Al_2O_3 even in a highly permeable architecture.

Enlarging the pore size from 800 to 1000 μm to 1000–1200 μm influences each composition differently. For the unreinforced alloy (C → E), the roughness coefficient drops modestly from 4.49 to 4.19 (≈7%), yet the corrosion current density J_{corr} plunges by 55%, indicating that larger pores promote a more uniform passive film and markedly reduce the overall corrosion rate. In contrast, the SiC-reinforced composite (SC → SE) experiences a similar decrease in R_f (4.48 → 4.11; ≈8%), but Jcorr more than doubles (+103%), showing that the additional electrolyte penetration provided by coarser pores favors the work of the corrosion microgalvanic cells of SiC particles and the Al matrix, overwhelming any benefit from the smoother surface. Finally, for the Al_2O_3-reinforced composite (AC → AE), a comparable 7% reduction in R_f (4.41 → 4.12) is accompanied by a 65% fall in J_{corr}, closely mirroring the trend of the unreinforced alloy and confirming that electrically inert Al_2O_3 does not trigger aggressive electrochemical interactions even when pore connectivity increases. This behavior is fully in support of studies reported by other authors regarding carbide [22–24] and oxide inclusions [28].

In order to evaluate the separate influence of the composite composition from that of the inner surface of the pores, the pores were sealed with an insulating resin. The results are presented in Table 1 (in parentheses). It is noted that in this case the OCP as well as the corrosion potentials are shifted significantly in a positive direction. This demonstrates that in the case of open pores a galvanic corrosion cell is created due to different access of oxygen, in which the anodic half-reaction is concentrated on the inner surface of the pores, and the outer surface, which is more accessible to the oxygen (dissolved in the electrolyte) plays the role of a cathode. The ratio of the corrosion current of porous samples to the corrosion current with sealed pores (I_{pore}/I_{sealed}) could be used as a criterion for assessing the share of the anodic surface in the interior of the pores. As expected, all samples show a ratio $I_{pore}/I_{sealed} > 1$, i.e., the current from the surface is less than the total current with the participation of the surface in the pores. However, if the decrease in current was solely the result of a decrease in the electrode surface area, then the ratio should be approximately equal to the factor R_f. However, the results show that these ratios I_{pore}/I_{sealed} are smaller than R_f (i.e., $I_{pore} >> I_{sealed}$), especially for the series of samples with narrower pores. This is probably due to the fact that in narrower pores the diffusion of oxygen is further hindered, which stimulates the operation of galvanic cells due to different access of oxygen.

3.2. Gravimetric Tests Results

The results of the gravimetric corrosion tests for the composites based on the AlSn6Cu alloy are depicted in Figure 5. Given the significant porosity of the examined materials and the consequent difficulty in precisely determining the actual corroded surface area, mass loss was adopted in the present study as a comparative parameter. This approach is justified by the direct proportionality between mass loss and the corrosion rate per unit area.

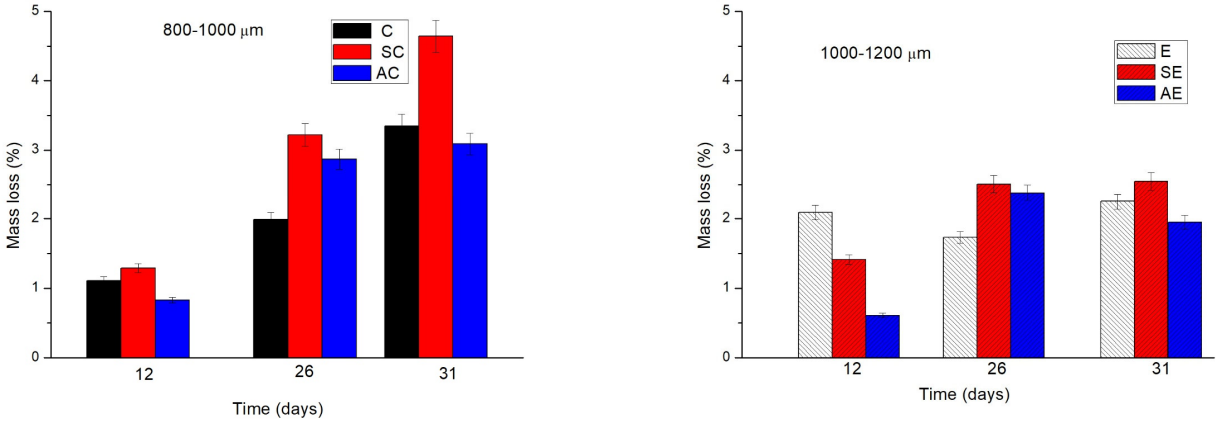

(**a**) (**b**)

Figure 5. Average mass loss of the of studied composite samples after the 12th, 26th and 31st days; (**a**) samples with pore size 800–1000 μm; (**b**) samples with pore size 1000–1200 μm.

Average mass-loss data from the 31-day gravimetric test confirm that both pore architecture and reinforcement chemistry govern the long-term stability of the open-cell AlSn6Cu materials. For the fine-pore specimens (800–1000 μm) the mass loss after 12 days is close and is in the range of 0.75–1.4%. However, during the next two time intervals, the unreinforced C and SiC-reinforced specimens corroded steadily (reaching 3.35% and 4.64%, respectively, at 31 days), while the AC corrosion stabilized, ending at only 3.09%. Thus, in the series of specimens with narrower pores, the SC composite remained with the highest mass loss. In other words, Al_2O_3 helps to stabilize the passive layer, whereas SiC continues to foster dissolution. In the large pore series (1000–1200 μm) within 12 days, sample E exhibited an increased mass loss (2.09%), while for SE and AE the value decreased slightly to 1.41% and 0.61%, respectively. During the removal of corrosion products, some non-corroded fine metal particles connected by narrow necks may also have been detached. Certain regions of the porous structure are connected by fragile necks that can weaken after prolonged exposure to the corrosive environment, which may partly explain the higher mass loss recorded for sample E after 12 days and for sample AE after 26 days. For sample E the initial decrease in mass loss can be associated with the formation of a non-uniform passive film that temporarily reduces dissolution. With continued immersion, this unstable layer locally breaks down in chloride solution, allowing renewed electrolyte access to the metallic surface and leading to a subsequent increase in mass loss. The higher overall porosity (compared to AE) further facilitates electrolyte penetration and accelerates localized corrosion, amplifying these fluctuations. For sample AE, the early stage shows an increase in mass loss, reflecting active dissolution of the matrix. In the following stage, however, the presence of Al_2O_3 particles contributes to the stabilization of corrosion products and supports the integrity of passive films. The lower porosity (compared to E) also reduces the effective surface area exposed to the electrolyte and limits the connectivity of corrosion paths. Together, these effects lead to a subsequent decrease in mass loss, consistent with reports on Al/Al_2O_3 composites exposed to chloride-containing environments [36,37]. In the later periods, the mass loss does not change significantly and remains below 2.5% for SE, confirming that in the larger pore architecture the influence of reinforcement type is weaker, although the SiC composite still exhibits the greatest cumulative damage. Comparable immersion studies on Al–Al_2O_3 composites also highlight the aggressive role of chloride environments. Singh et al. [38] reported the highest corrosion rate for a 6061/Al_2O_3 composite after 20 h of immersion in HCl solution, attributing the degradation to chloride ions disrupting and removing the protective alumina film. They further observed that the

corrosion rate decreased with longer immersion times. A similar tendency is observed for our open-cell composites (E, SE, AE), where the mass loss curves flatten between days 26 and 31, indicating a slowing corrosion rate. By contrast, the control sample (C) continues to exhibit a steady increase in mass loss over time.

Comparing the same composition across pore sizes reveals a clear pattern. Enlarging the pores lowers the final 31-day mass loss for every system—by 33% for the unreinforced alloy (3.35% → 2.25%), by 45% for the SiC composite (4.64% → 2.55%) and by 37% for the Al_2O_3 composite (3.09% → 1.95%). These results echo the polarization data and confirm the operation of two types of galvanic cells—due to different compositions and to different oxygen access levels. The larger pores tend to mitigate corrosion provided the reinforcement is not galvanically active, while SiC continues to impose a penalty by sustaining higher dissolution rates even when cumulative loss is reduced.

To verify the claim of formation of microgalvanic corrosion elements, the surface of the samples was observed by SEM before and after the corrosion gravimetric tests (Figure 6). The initial surface of the carbide-reinforced alloy is more inhomogeneous compared to that of Al_2O_3. After prolonged exposure to 3.5% NaCl, the surface under the corrosion products is severely corroded to the formation of microcavities. The cavities in the oxide reinforcement appear shallower. However, such roughening is typical of microgalvanic corrosion elements due to inhomogeneous composition or non-metallic inclusions.

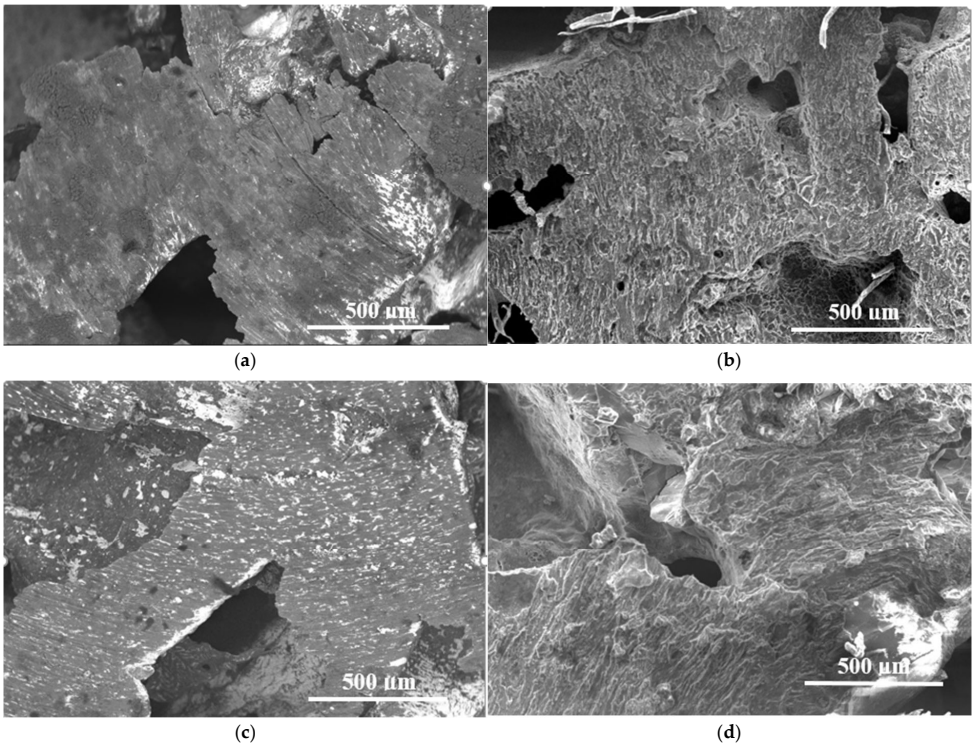

(**a**) (**b**) (**c**) (**d**)

Figure 6. SEM images of surface of AlSn6Cu alloy reinforced with SiC (**a**,**b**) and with Al_2O_3 (**c**,**d**) before (**a**,**c**) and after (**b**,**d**) gravimetric corrosion test.

The comparison of the elemental composition of the samples before and after the corrosion test shows enrichment of the surface with the elements Sn and Cu (Table 2). The strongest attack is suffered by aluminum, which has the most negative potential. The contact of aluminum with cathodic impurities (such as copper, tin and SiC) maintains it in an active state and prevents the formation of protective passive layers in a chloride environment.

Table 2. EDS normalized values of the elements Al, Sn and Cu on the surfaces before and after corrosion gravimetric tests.

Reinforcement:	**SiC**		**Al_2O_3**	
	Before Corr. Test	**After Corr. Test**	**Before Corr. Test**	**After Corr. Test**
Al [mass. %]	82.8	75.4	81.4	72.4
Sn [mass. %]	12.5	20.0	17.2	24.1
Cu [mass. %]	1.8	3.3	1.4	3.5
Si [mass. %]	2.9	1.2	-	-

After corrosion testing and subsequent repeated washing with hot water and HNO_3 until a constant weight was achieved according to the procedure in ASTM G1, the samples were observed using SEM (Figure 7). These observations revealed that the interior pore walls are covered with an uneven, porous, whitish layer, likely consisting of the main corrosion products. Two distinct morphologies of corrosion products were identified: (i) dense, short, rod-like structures, denoted 1 (Figure 7a,c,d,f) and (ii) thin, light, ribbon-like formations, denoted 2 (Figure 7b,c,e,f).

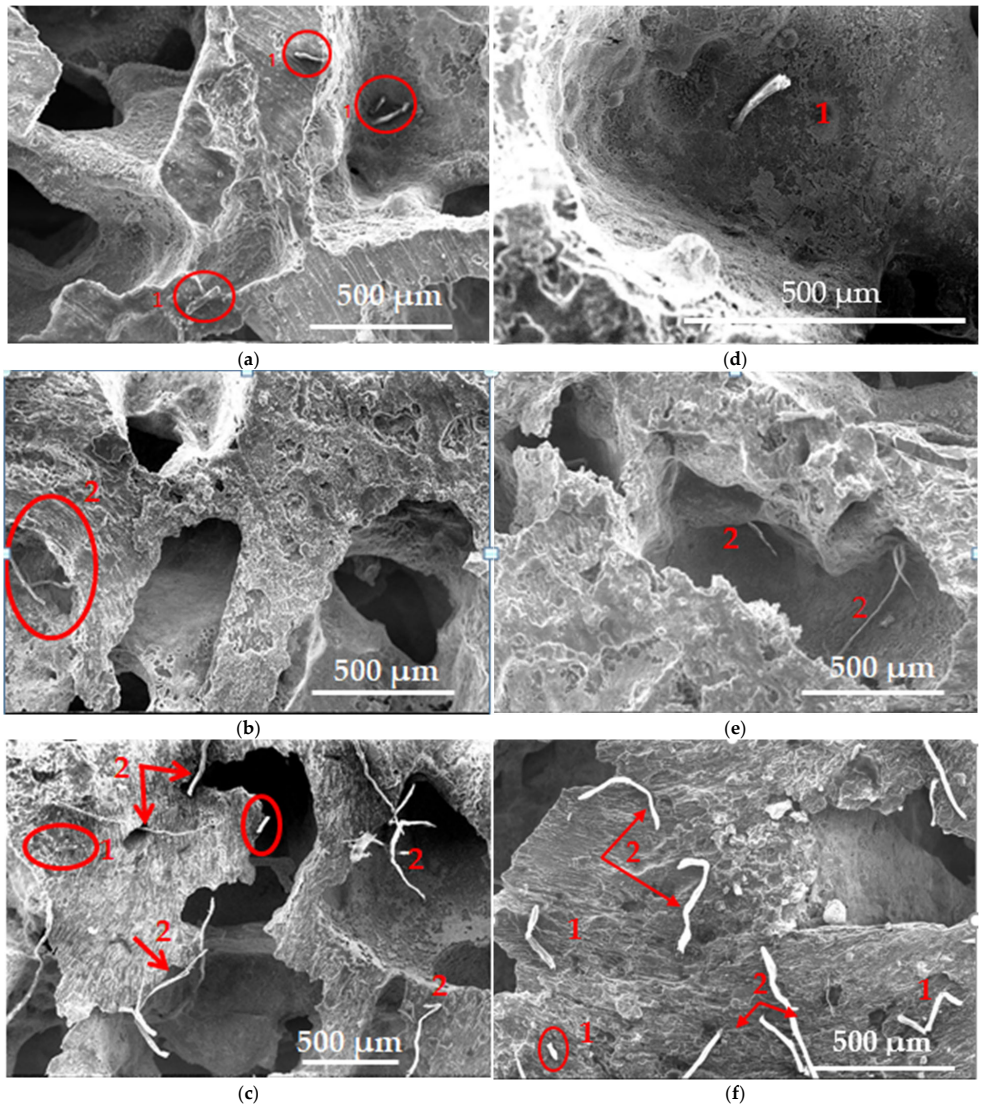

Figure 7. SEM images of open-cell AlSn6Cu materials and its composites after gravimetric corrosion test: (**a**) unreinforced C; (**b**) reinforced SC; (**c**) reinforced AC; (**d**) unreinforced E; (**e**) reinforced SE; (**f**) reinforced AE.

The thin, ribbon-like formations were observed exclusively in the reinforced specimens, appearing predominantly around the pore boundaries—a phenomenon likely related to the composite fabrication method [29]. Energy-dispersive EDS analysis revealed that these formations consist solely of aluminum and oxygen (Figure 8b). In contrast, the short, rod-like structures were located at the bottom of the pores and were composed primarily of Al and Sn, with minor traces of Cu (Figure 8a). These findings are consistent with previous reports [39], which attributed similar features to the pitting corrosion of SiC-reinforced aluminum matrix composites after prolonged immersion in NaCl solution.

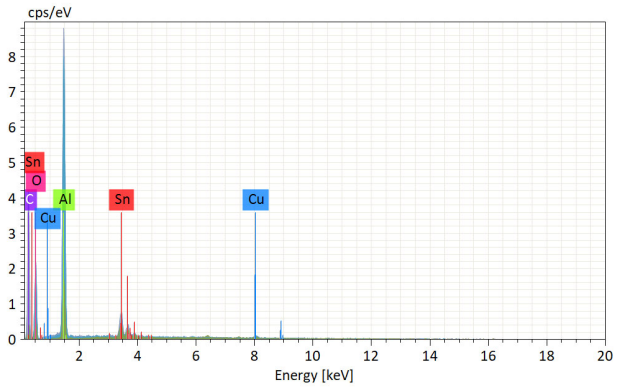

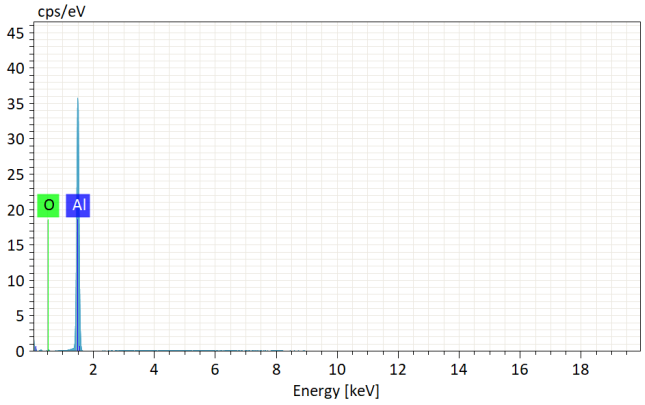

Al, [mass. %]	Sn [mass. %]	Cu, [mass. %]
82.77	15.65	1.58

(**a**)

Al, [mass. %]	O, [mass. %]	Cu, [mass. %]
97.16	2.84	-

(**b**)

Figure 8. EDS analysis results (in mass norm. %) for the formations highlighted in the SEM micrographs (Figure 7): (**a**) rod-like formations, denoted 1 (Figure 7a). (**b**) white ribbon-like formations, denoted 2 (Figure 7b).

The phase composition of the corroded specimens was determined by X-ray diffraction (XRD) (Figure 9). The analysis revealed the presence of several types of phases: oxides, chlorides, complex oxychlorides, and elemental phases. The intensity of the diffraction peaks corresponding to the primary elemental phases Al and Sn in the specimens with pore sizes of (800 ÷ 1000) μm (Figure 9a) was nearly identical in samples C and AC, but significantly higher in SC, indicating a greater concentration of these phases in the latter. In the specimens with pore sizes of (1000 ÷ 1200) μm (Figure 9b), the main diffraction peaks of Al and Sn were more intense in E and AE, and lower in SE. The NaCl phase at $2\theta = 44.9°$ was identified in the XRD-patterns of all composites, which can be attributed either to the retained electrolyte within the pores during the corrosion test or to NaCl crystals used in the preparation of the composites.

The Cu_2O phase ($2\theta = 45.5°$) was identified in all tested specimens except for the unreinforced sample E. A second copper-containing phase, CuCl, with a peak at $2\theta = 30.5°$, was detected in all specimens except the unreinforced sample C. The diffraction peak of this phase was most intense in sample E.

XRD-patterns confirmed that $Sn_3O(OH)_2Cl_2$, a complex oxide-chloride-hydroxide, was formed as a corrosion product of Sn after the gravimetric test [40]. This phase was present in all six composites; however, in those with pore sizes of (800–1000) μm, the peaks exhibited low intensity, suggesting a smaller quantity.

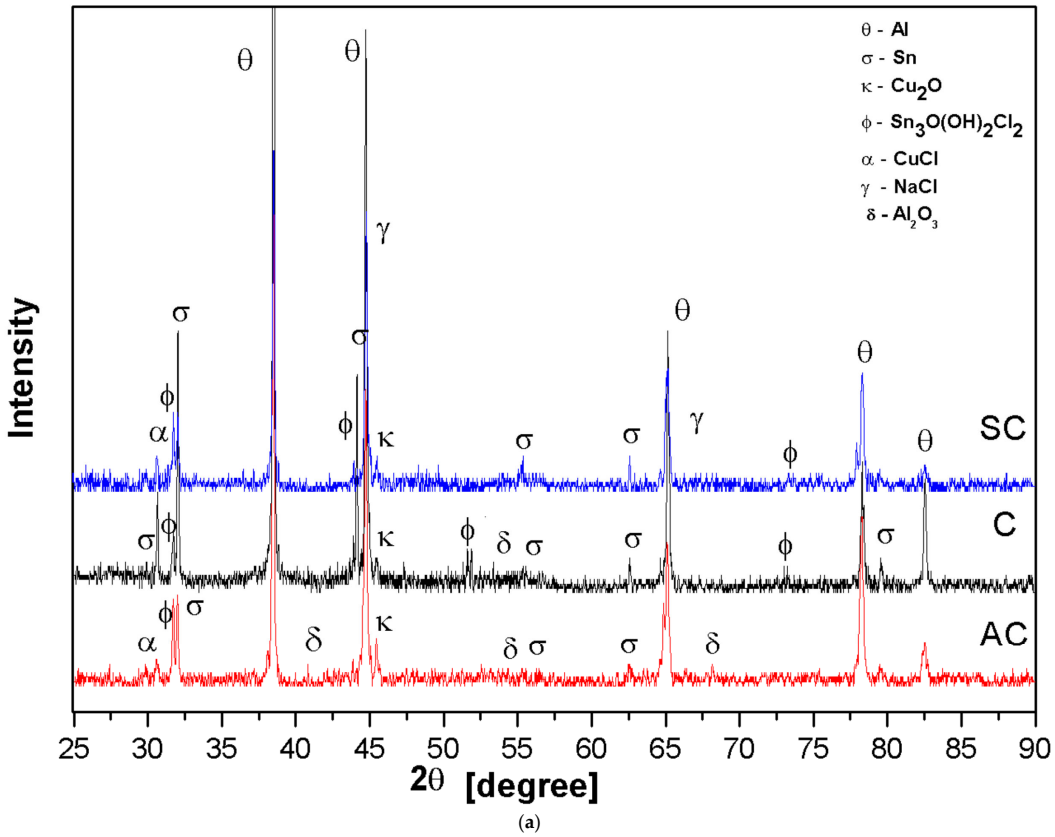

(**a**)

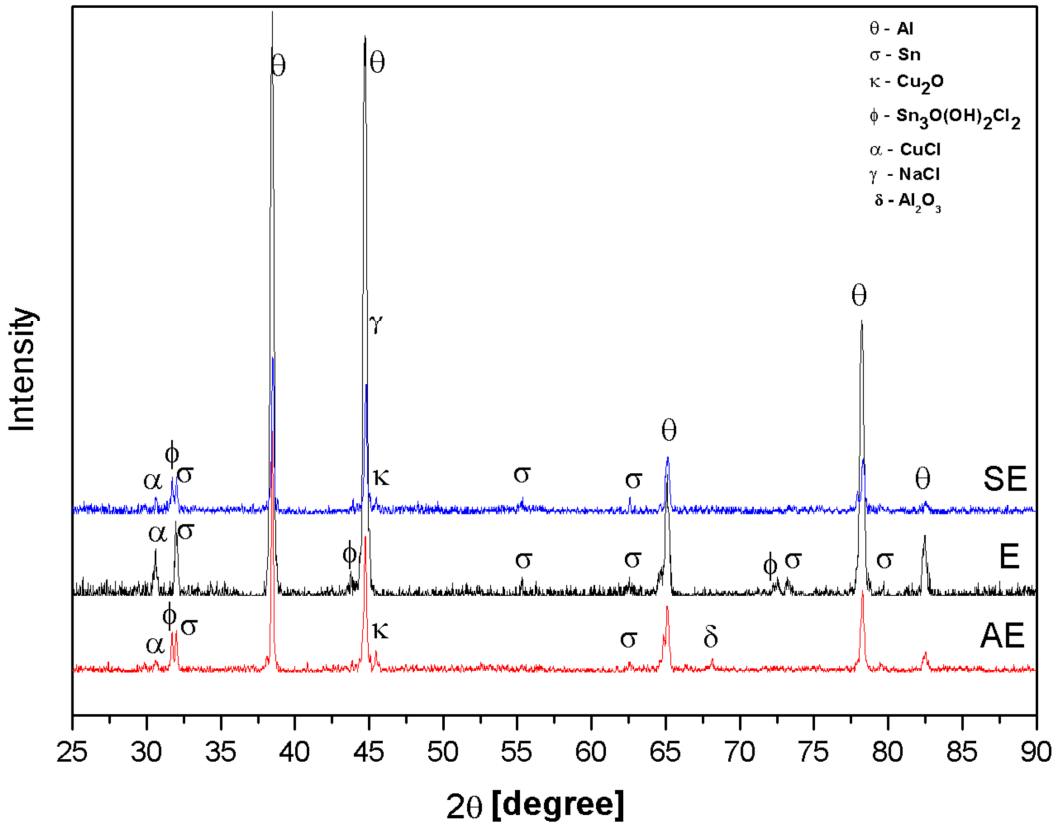

(**b**)

Figure 9. X-ray diffraction patterns of open-cell AlSn6Cu and its composites after immersion corrosion testing: (**a**) samples with pore size 800–1000 μm; (**b**) samples with pore size 1000–1200 μm. Phase identification is based on JCPDS reference files: Al (04-0787), Sn (04-0673), NaCl (05-0628), Cu_2O (05-0667), CuCl (06-0344), Al_2O_3 (46-1212), $Sn_3O(OH)_2Cl_2$ (39-0314).

Aluminum exhibits the highest reactivity among the three base metals in the AlSn6Cu alloy. Consequently, it is assumed that under exposure to a corrosive electrolytic environment, aluminum is the primary element involved in the anodic reaction. It is well known that Al_2O_3 possesses good dielectric properties and an amorphous structure, which explains both the light color of the corrosion products observed in the SEM images and the absence of diffraction peaks in the XRD pattern. The other two elements—tin and copper—and their respective oxides exhibit semiconducting properties and can act as cathodic impurities within the aluminum matrix, thereby promoting its dissolution. However, in the Al_2O_3-reinforced composite, the volume fraction of Al_2O_3 exceeds that of the base matrix. This suggests that over time, the accumulation of Al_2O_3 corrosion products may clog the pores. As a result, the matrix's contact area with the electrolyte progressively decreases, which in turn leads to a reduction in the corrosion rate. This behavior is particularly well supported by the gravimetric data for sample E (with larger pores), where the corrosion process occurs mainly in the early stages of testing. After this initial period, mass loss stabilizes, indicating that no significant new corrosion products are formed over time.

The lower corrosion resistance observed in sample C can be attributed to effects that are more pronounced in narrower and deeper pores and crevices, including: (i) formation of highly active anodic zones; (ii) increased chloride ion concentration, which favors the formation of $AlCl_3$—a compound lacking the protective qualities of Al_2O_3; (iii) acidification within the pores; and (iv) other mechanisms characteristic of pitting and crevice corrosion.

The varying influence of the reinforcing particles on the corrosion behavior of the base alloy is primarily determined by their intrinsic nature. On one hand, due to their dielectric properties and high chemical inertness, Al_2O_3 particles can be considered inert with respect to the AlSn6Cu matrix. As such, they do not alter the matrix's surface electrochemically, and the observed reduction in corrosion rate upon their addition is attributed to a decreased effective surface area exposed to the electrolyte [41]. On the other hand, carbides such as SiC are typically regarded as cathodic non-metallic inclusions. These particles promote the dissolution of the metal matrix at the carbide/matrix interface by preventing passivation and maintaining the metal in an active state [41]. Therefore, SiC particles act as persistent corrosion stimulators—an effect confirmed by our results.

4. Conclusions

Open-cell AlSn6Cu materials and their SiC- and Al_2O_3-reinforced counterparts were successfully fabricated via liquid-state processing with controlled pore sizes of 800–1000 μm and 1000–1200 μm. The resulting materials exhibited total porosities ranging from 36% to 66%, with comparable surface roughness coefficients (R_f = 4.1–4.5), enabling a consistent basis for evaluating corrosion behavior.

In both pore regimes, the Al_2O_3-reinforced composite demonstrated the most favorable electrochemical performance, achieving the lowest corrosion current density (J_{corr} = 4.01 μA cm^{-2} for AE with 1000–1200 μm pores), with only a modest increase observed in the finer-pore variant (11.4 μA cm^{-2} for AC). By contrast, SiC reinforcement led to a marked deterioration in corrosion resistance, with the highest J_{corr} value recorded for SE (37.9 μA cm^{-2}), indicating that SiC promotes aggressive galvanic activity regardless of surface morphology. A closer analysis of pore size effects within each composition reveals that for the unreinforced alloy (C → E), increasing the pore size from 800 to 1000 μm to 1000–1200 μm reduced R_f by 7% (from 4.49 to 4.19) and decreased J_{corr} by 55% (from 10.6 to 4.80 μA cm^{-2}), suggesting improved passive film stability in more open structures. A similar trend was observed for the Al_2O_3-reinforced composite (AC → AE), where a 7% drop in R_f (4.41 to 4.12) corresponded to a 65% reduction in J_{corr} (11.4 to 4.01 μA cm^{-2}). Conversely, the SiC-reinforced composite (SC → SE) showed the opposite behavior: despite an 8%

reduction in R_f (4.48 to 4.11), J_{corr} more than doubled (18.7 to 37.9 μA cm^{-2}), indicating that the larger pores intensified the work of corrosion microgalvanic cells between SiC particles and the aluminum matrix.

Gravimetric immersion data for 31 days corroborated the electrochemical trends. In the fine-pore group, cumulative mass loss ranked C < AC < SC (3.35, 3.09 and 4.64%, respectively), whereas in the coarse-pore group, it ranked AE < E < SE (1.95, 2.25 and 2.55%). Moving from fine to coarse pores reduced the 31-day mass loss by 33% for the unreinforced alloy, 37% for the Al_2O_3 composite and 45% for the SiC composite, yet SiC remained the least durable overall. Notably, the Al_2O_3-reinforced specimens combined the lowest final mass losses with the lowest J_{corr} values, confirming their superior long-term stability.

Since the variation in R_f across all specimens remained within a narrow 9% range, surface roughness alone cannot account for the wide disparity in corrosion rates. Instead, reinforcement chemistry, particularly the presence of galvanically active vs. inert ceramic phases, plays a dominant role in determining corrosion behavior.

Overall, optimal corrosion resistance in open-cell AlSn6Cu materials is achieved through the combination of a coarser-pore architecture (1000–1200 μm) and Al_2O_3 reinforcement. This pairing minimizes electrochemical activity and supports the development of a more stable passive layer. In contrast, SiC reinforcement, especially in larger-pore composites, should be avoided due to its tendency to promote localized galvanic corrosion, negating any benefit from decreased roughness or porosity.

Author Contributions: Conceptualization, M.K. and V.D.; methodology, M.K., Y.K., B.T., H.S., V.D. and R.D.; formal analysis, M.K., Y.K., B.T., H.S., V.D. and R.D.; investigation, Y.K., B.T., H.S., V.D. and R.D.; resources, M.K., Y.K., B.T., H.S., V.D. and R.D.; writing—original draft preparation, V.D., Y.K. and B.T.; writing—review and editing, M.K., V.D. and B.T.; visualization, Y.K., B.T., H.S., V.D. and R.D.; supervision, M.K. and V.D.; project administration, M.K.; funding acquisition, M.K. All authors have read and agreed to the published version of the manuscript.

Funding: This research was funded by the Bulgarian National Science Fund, Project КП-06-Н57/20 'Fabrication of new type of self-lubricating antifriction metal matrix composite materials with improved mechanical and tribological properties'.

Institutional Review Board Statement: Not applicable.

Informed Consent Statement: Not applicable.

Data Availability Statement: The original contributions presented in this study are included in the article. Further inquiries can be directed to the corresponding author.

Acknowledgments: This work was supported by European Regional Development Fund under "Research Innovation and Digitization for Smart Transformation" program 2021-2027 under the Project BG16RFPR002-1.014-0006 "National Centre of Excellence Mechatronics and Clean Technologies".

Conflicts of Interest: The authors declare no conflicts of interest.

References

1. Banhart, J. Manufacture, Characterisation and Application of Cellular Metals and Metal Foams. *Prog. Mater. Sci.* **2001**, *46*, 559–632. [CrossRef]
2. Ashby, M.F.; Evans, A.G.; Fleck, N.A.; Gibson, L.J.; Hutchinson, J.W.; Wadley, H.N.G. *Metal Foams: A Design Guide*; Butterworth-Heinemann: Boston, MA, USA, 2000.
3. Duarte, I.; Ferreira, J.M.F. Aluminium Alloy Foams: Production and Properties. *J. Mater. Process. Technol.* **2004**, *148*, 152–158. [CrossRef]
4. Zhao, J.; Li, Q. Effect of magnetic-mechanical coupled stirring on the distribution of B4C particles in Al-B4C composites. *J. Mater. Eng. Perform.* **2022**, *31*, 907–917. [CrossRef]
5. Agrawal, E.; Tungikar, V. Wear performance of Al-TiC composite at elevated temperature. *World J. Eng* **2021**, *19*, 346–351. [CrossRef]

6. Samal, P.; Vundavilli, P.R.; Meher, A.; Mahapatra, M.M. Multi-response modeling for sliding wear behavior of AA5052/TiC composites by stir casting: A comparative analysis using response surface methodology and fuzzy logic system. *Proc. Inst. Mech. Eng. E J. Process Mech. Eng.* **2022**, *236*, 254–266. [CrossRef]
7. Alam, M.A.; Ya, H.H.; Azeem, M.; Yusuf, M.; Sapuan, S.M.; Masood, F. Investigating the effect of mixing time on the crystallite size and lattice strain of the AA7075/ TiC composites. *Mater. Werkst.* **2021**, *52*, 1112–1120. [CrossRef]
8. Turan, M.E.; Aydin, F.; Sun, Y.; Zengin, H.; Akinay, Y. Wear resistance and tribo logical properties of GNPs and MWCNT reinforced AlSi18CuNiMg alloys produced by stir casting. *Tribol. Int.* **2021**, *164*, 107201. [CrossRef]
9. Zhang, H.; Zhang, B.; Gao, Q.; Song, J.; Han, G. A review on microstructures and properties of graphene-reinforced aluminum matrix composites fabricated by friction stir processing. *J. Manuf. Process.* **2021**, *68*, 126–135. [CrossRef]
10. Chintada, S.; Dora, S.P.; Kare, D. Mechanical behavior and metallographic characterization of microwave sintered Al/SiC composite materials–an experimental approach. *Silicon* **2022**, *14*, 7341–7352. [CrossRef]
11. Kumar, K.; Dabade, B.; Wankhade, L. Determination of prediction model and optimization of process parameters for fabrication of Al-SiC composite using response surface methodology. *Adv. Mater. Process. Technol.* **2022**, *8*, 1983–1999. [CrossRef]
12. Baghel, M.; Krishna, C.M.; Suresh, S. Development of Al-SiC composite material from rice husk and its parametric assessment. *Mater. Res. Express* **2022**, *9*, 016518. [CrossRef]
13. Zabihi, M.; Qods, F.; Emadoddin, E. The effect of simple shear extrusion on the texture and porosity content of Al/Al_2O_3 composites. *Iran. J. Mater. Form.* **2022**, *9*, 26–35. [CrossRef]
14. Dang, X.; Zhang, B.; Zhang, Z.; Hao, P.; Xu, Y.; Xie, Y.; Huang, R.; Wang, K.; Wang, W.; Wang, Q. Microstructural evolutions and mechanical properties of multilayered 1060Al/Al-Al_2O_3 composites fabricated by cold spraying and accumulative roll bonding. *J. Mater. Res. Technol* **2021**, *15*, 3895–3907. [CrossRef]
15. Aydin, F. The investigation of the effect of particle size on wear performance of AA7075/Al_2O_3 composites using statistical analysis and different machine learning methods. *Adv. Powder Technol.* **2021**, *32*, 445–463. [CrossRef]
16. Eifert, H.; Banhart, J. Metal Foams in Strongly Corrosive Environments. In *Cellular Metals: Manufacture, Properties, and Applications*; Banhart, J., Fleck, N.A., Mortensen, A., Eds.; MIT-Verlag: Bremen, Germany, 2003; pp. 231–236.
17. Chan, H.L.; Guo, K. Corrosion Studies of Open Cell Aluminum Foam in Simulated Marine Environment. Cal State ScholarWorks. 2020. Available online: https://scholarworks.calstate.edu/concern/projects/ht24wm58j (accessed on 25 July 2025).
18. Rossi, S.; Calovi, M.; Fedel, M. Corrosion Protection of Aluminum Foams by Cataphoretic Deposition. *Surf. Coat. Technol.* **2017**, *307*, 100–107. [CrossRef]
19. Liu, J.; Zhu, X.; Sudagar, J.; Gao, F.; Feng, P. Preparation and Corrosion Resistance of Electroless Ni-P Coating on Open-Cell Aluminum Foams. *Int. J. Electrochem. Sci.* **2012**, *7*, 5951–5961. [CrossRef]
20. Hihara, L.H.; Latanision, R.M. Corrosion of metal matrix composites. *Int. Mater. Rev.* **1994**, *39*, 245–264. [CrossRef]
21. Ikubanni, P.; Oki, M.; Adeleke, A.; Adesina, O.; Omoniyi, P.; Akinlabi, E. Electrochemical Studies of the Corrosion Behavior of Al/SiC/PKSA Hybrid Composites in 3.5% NaCl Solution. *J. Compos. Sci.* **2022**, *6*, 286. [CrossRef]
22. Mahdi, S.M.; Ghalib, L. Corrosion behavior of Al/SiC composite prepared by powder metallurgy in chloride environments. *J. Bio-Tribo-Corros.* **2022**, *8*, 8. [CrossRef]
23. Loto, R.T.; Babalola, P. Analysis of SiC grain size variation and NaCl concentration on the corrosion susceptibility of AA1070 aluminium matrix composites. *Cogent Eng.* **2018**, *5*, 1473002. [CrossRef]
24. Nunes, P.C.R.; Ramanathan, L.V. Corrosion behavior of alumina-aluminum and silicon carbide-aluminum metal-matrix composites. *Corrosion* **1995**, *51*, 610–617. [CrossRef]
25. Erdemir, F.; Canakci, A.; Varol, T.; Ozkaya, S. Corrosion and wear behavior of functionally graded Al2024/SiC composites produced by hot pressing and consolidation. *J. Alloys Compd.* **2015**, *644*, 589–596. [CrossRef]
26. Candan, S.; Bilgic, E. Corrosion behavior of Al–60 vol.% SiCp composites in NaCl solution. *Mater. Lett.* **2004**, *58*, 2787–2790. [CrossRef]
27. Loto, R.T.; Babalola, P. Evaluation of the influence of alumina nano-particle size and weight composition on the corrosion resistance of monolithic AA1070 aluminium. *Mater. Today Proc.* **2022**, *65*, 2138–2143. [CrossRef]
28. Natishan, P.M.; O'grady, W.E. Chloride ion interactions with oxide-covered aluminum leading to pitting corrosion: A review. *J. Electrochem. Soc.* **2014**, *161*, 421–432. [CrossRef]
29. Kolev, M.; Drenchev, L.; Petkov, V.; Dimitrova, R.; Kovacheva, D. Open-Cell AlSn6Cu-SiC Composites: Fabrication, Dry-Sliding Wear Behavior, and Machine Learning Methods for Wear Prediction. *Materials* **2023**, *16*, 6208. [CrossRef] [PubMed]
30. Kolev, M.; Drenchev, L.; Petkov, V.; Dimitrova, R.; Kolev, K.; Simeonova, T. Fabrication and Dry-Sliding Wear Characterization of Open-Cell AlSn6Cu–Al_2O_3 Composites with LSTM-Based Coefficient of Friction Prediction. *Metals* **2024**, *14*, 428. [CrossRef]
31. *ASTM G1-03(2017)e1*; Standard Practice for Preparing, Cleaning, and Evaluating Corrosion Test Specimens. ASTM International: West Conshohocken, PA, USA, 2025.
32. Zhang, X.L.; Jiang, Z.H.; Yao, Z.P.; Song, Y.; Wu, Z.D. Effects of scan rate on the potentiodynamic polarization curve obtained to determine the Tafel slopes and corrosion current density. *Corros. Sci.* **2009**, *51*, 581. [CrossRef]

33. Zhou, H.; Chhin, D.; Morel, A.; Gallant, D.; Mauzeroll, J. Potentiodynamic polarization curves of AA7075 at high scan rates interpreted using the high field model. *Npj Mater. Degrad.* **2022**, *6*, 20. [CrossRef]
34. Xie, X.; Holze, R. Electrode Kinetic Data: Geometric vs. Real Surface Area. *Batteries* **2022**, *8*, 146. [CrossRef]
35. Wu, L.; He, Y.-H.; Jiang, Y.; Zeng, Y.; Xiao, Y.-F.; Nan, B. Effect of pore structures on corrosion resistance of porous Ni3Al intermetallics. *Trans. Nonferrous Met. Soc. China* **2014**, *24*, 3509–3516. [CrossRef]
36. Vini, M.H.; Daneshmand, S.; Alabboodi, K.O.; Ali, A.B.M.; Jasim, D.J.; Salahshour, S.; Hekmatifar, M. Corrosion and Mechanical Properties of Al/Al_2O_3 Composites Fabricated via Accumulative Roll Bonding Process: Experimental and Numerical Simulation. *Surf. Coat. Technol.* **2024**, *494*, 131370. [CrossRef]
37. Aydın, F. A Review of Recent Developments in the Corrosion Performance of Aluminium Matrix Composites. *J. Alloys Compd.* **2023**, *949*, 169508. [CrossRef]
38. Prathap Singh, S.; Ananthapadmanaban, D.; Arun Vasantha Geethan, K.; Ravichandran, P. Microscopical and Corrosion Studies on Al6061—10% Al_2O_3 Functionally Graded Metal Matrix Composites. *Mater. Today* **2022**, *62*, 459–462. [CrossRef]
39. Yu, L.; Hao, S.; Nong, X.; Cao, X.; Zhang, C.; Liu, Y.; Yan, Y.; Jiang, Y. Comparative Study on the Corrosion Resistance of 6061Al and SiC3D/6061Al Composite in a Chloride Environment. *Materials* **2021**, *14*, 7730. [CrossRef]
40. Roberge, P.R. *Corrosion Engineering: Principles and Practice*, 1st ed.; McGrawHill: New York, NY, USA, 2008.
41. Karthikraja, M.; Ramanathan, K.; Loganathan, K.T.; Selvaraj, S. Corrosion behaviour of SiC and Al_2O_3 reinforced Al 7075 hybrid aluminium matrix composites by weight loss and electrochemical methods. *J. Indian Chem. Soc.* **2023**, *100*, 101002. [CrossRef]

Disclaimer/Publisher's Note: The statements, opinions and data contained in all publications are solely those of the individual author(s) and contributor(s) and not of MDPI and/or the editor(s). MDPI and/or the editor(s) disclaim responsibility for any injury to people or property resulting from any ideas, methods, instructions or products referred to in the content.